crystals

MDPI

Article

Effect of Hot-Rolling on the Microstructure and Impact Toughness of an Advanced 9%Cr Steel

Evgeniy Tkachev [1,2,*], Andrey Belyakov [1] and Rustam Kaibyshev [2]

[1] Laboratory of Mechanical Properties of Nanostructured Materials and Superalloys, Belgorod State University, 308015 Belgorod, Russia
[2] Laboratory of Advanced Steels for Agricultural Machinery, Russian State Agrarian University—Moscow Timiryazev Agricultural Academy, 127550 Moscow, Russia
* Correspondence: tkachev_e@bsu.edu.ru; Tel.: +7-4722-565457

Abstract: A 9%Cr martensitic steel with Ta and B additions was subjected to thermo-mechanical treatment (TMT) including rolling in the range of metastable austenite at 900–700 °C followed by water quenching and tempering at different temperatures. Applied TMT with tempering at T ≥ 700 °C substantially improved the impact toughness. The application of the TMT with subsequent tempering at 780 °C decreased the ductile–brittle transition temperature from 40 to 15 °C and increased the upper shelf energy from 300 to 380 J/cm^2 as compared to the normalized and tempered (NT) condition. The microstructural observations with scanning and transmission electron microscopes showed the precipitation of fine Ta-rich MX carbonitride and $M_{23}C_6$ carbide during TMT and subsequent tempering. The analysis of the cleavage facets and the secondary cracks with electron back-scattered diffraction (EBSD) revealed that the brittle fracture occurred via cleavage cracking along {100} planes across the laths, while the high-angle boundaries of martensite blocks and packets were effective barriers to the crack propagation. The increased impact toughness of the tempered TMT steel sample was attributed to enhanced ductile fracture owing to the uniform dispersion of the precipitates and favorable {332}⟨113⟩ crystallographic texture.

Keywords: high-Cr martensitic steels; electron microscopy; mechanical characterization; ductile–brittle transition; grain and interfaces; fracture behavior

Citation: Tkachev, E.; Belyakov, A.; Kaibyshev, R. Effect of Hot-Rolling on the Microstructure and Impact Toughness of an Advanced 9%Cr Steel. *Crystals* **2023**, *13*, 492. https://doi.org/10.3390/cryst13030492

Academic Editor: Tomasz Sadowski

Received: 26 February 2023
Revised: 6 March 2023
Accepted: 10 March 2023
Published: 12 March 2023

1. Introduction

High-chromium martensitic steels are the main structural materials used in the steam circuit of modern power units due to their relatively high creep strength, good oxidation resistance at elevated temperatures and low cost [1–3]. In recent decades, significant efforts have been made to the development of advanced 9–12%Cr steels with increased boron content. The improved creep strength of these steel grades is mainly attributed to the pinning effect from the finely dispersed $M_{23}C_6$ carbide and MX carbonitride (M—metal; X—C/N) particles precipitated along the grain boundaries and characterized by low coarsening rate at the elevated temperature [1,4–6]. The enrichment of $M_{23}C_6$ carbides by B enhances their coarsening resistance under creep and aging conditions [7–10]. This effect was considered as a result of decreased surface energy of the $M_{23}(C,B)_6$/Ferrite interfaces [7,10,11]. It should be noted that the boron is a strong nitride-forming element and may form coarse BN particles in steels with standard N content of 500 ppm [12]. Thus, the nitrogen content should be controlled to prevent the formation of an undesirable brittle BN phase. The balanced content of B = 130 ppm and N = 70 ppm was shown as a promising alloying concept to increase the stability of $M_{23}C_6$ carbides without the formation of BN particles and to provide improved creep strength [6,10,13]. However, these steels were often found to be highly susceptible to brittle fracture at room temperature after conventional normalizing and tempering treatment [14–18]. To improve the impact toughness, these steels are usually subjected to tempering at higher temperatures (760–780 °C vs. 750–760 °C) compared to

the widely used commercial steels such as P91 and P92 [14,15,18,19]. It was suggested that the high density of $M_{23}C_6$ carbides located at the lath and block boundaries provoke brittle fracture while spheroidization and coarsening of these particles may enhance the Charpy impact energy [15]. Yan et. al. reported that the improvement of the toughness with increasing tempering temperature can be also attributed to a decrease of the dislocation density and the degree of supersaturation of interstitial atoms [14]. An increase in the tempering temperature leads to the pronounced coarsening of precipitates and widening of martensitic laths, thereby limiting the potential for an increase in creep resistance. Hence, the developing of an effective processing method for improving both the impact toughness and the distribution of secondary precipitations is of great importance.

Many studies have attempted to improve the mechanical properties of high-chromium martensitic steels by applying thermo-mechanical processing [20–25]. These works actually achieved considerable improvement in creep strength associated with the strengthening effect caused by finer laths and smaller precipitates [20,22–25]. Hot rolling in the non-recrystallization temperature region of γ-phase followed by water quenching was shown to produce a high density of dislocations which could serve as additional nucleation sites for precipitates and thus affects the particle dispersion [20,25–27]. Moreover, the development of various crystallographic textures during deformation, recrystallization and transformation may significantly influence the mechanical properties, especially, impact toughness [20,28–30]. Some of textures of controlled rolled steels, such as $\{332\}\langle 113\rangle$ and $\{554\}\langle 225\rangle$, were found particularly beneficial for the strength and toughness [28,30,31]. Thus, hot-rolling can be considered as promising method to provide the desirable fine-grained microstructure, and improved mechanical properties of high-chromium martensitic steels.

Since the steel grades with a modified balance of B and N have been developed recently, there are limited data regarding the effect of hot-rolling and subsequent tempering on their microstructure and mechanical properties. Therefore, the purpose of the present study is to investigate the relationship between the microstructure and impact toughness in the advanced 9%Cr steel with increased boron content subjected to different thermal and thermo-mechanical treatments. The influence of the secondary precipitates and crystallographic texture on the fracture behavior with regard to that of the tempering temperatures is discussed.

2. Materials and Methods

A 50 kg ingot of the studied 9%Cr steel was produced by vacuum induction melting. The chemical composition of the steel is given in Table 1. The alloying design of the steel is similar to that of commercial P92 grade. In this steel the boron and nitrogen contents were adjusted to 120 ppm and 70 ppm, respectively, and Ta was added to enhance the dispersion of the $M_{23}C_6$ and MX precipitates [32]. Two bars with dimensions 200 × 100 × 50 mm^3 were homogenized at 1200 °C for 12 h followed by multidirectional hot forging. Then the steel bars were subjected to the thermal and thermo-mechanical treatments as follows:

(1) Austenitization at 1050 °C for 30 min, air cooling (hereafter denoted as NT).
(2) Austenitization at 900 °C for 90 min, hot rolling with total reduction of 40%, water quenching (hereafter denoted as HR+Q).

Table 1. Chemical composition of the studied steel (wt.%).

C	Si	Mn	Cr	Co	Mo	W	V	Nb	Ni	B	N	Ta	Fe
0.11	0.03	0.31	9.05	3.03	0.60	1.99	0.20	0.06	0.02	0.013	0.007	0.085	Bal.

The NT and HR+Q samples were cut into 60 × 21 × 21 mm^3 (length × width × thickness) pieces and tempered at different temperatures ranging from 300 to 800 °C for 3 h. The specimens with a gauge length of 16 mm, a width of 3 mm and a thickness of 1.5 mm were

prepared for tensile tests. The tensile tests were performed at room temperature using an Instron 5882 testing machine at a constant loading rate of 1 mm/min. The impact tests were carried out on standard Charpy specimens of $10 \times 10 \times 55$ mm^3 with a 2 mm V-notch using an Instron IMP460 impact testing machine equipped with an Instron Dynatup Impulse data acquisition system. The load on the specimens during impact tests was continuously recorded as a function of the deflection. The orientation and dimensions of the tensile and Charpy specimens are sketched in Figure 1 along with the heat treatment and thermo-mechanical treatment schemes. The ductile–brittle transition temperature (DBTT) was determined as a temperature corresponding to the half value of the sum of the upper shelf energy (USE) and the lower shelf energy (LSE).

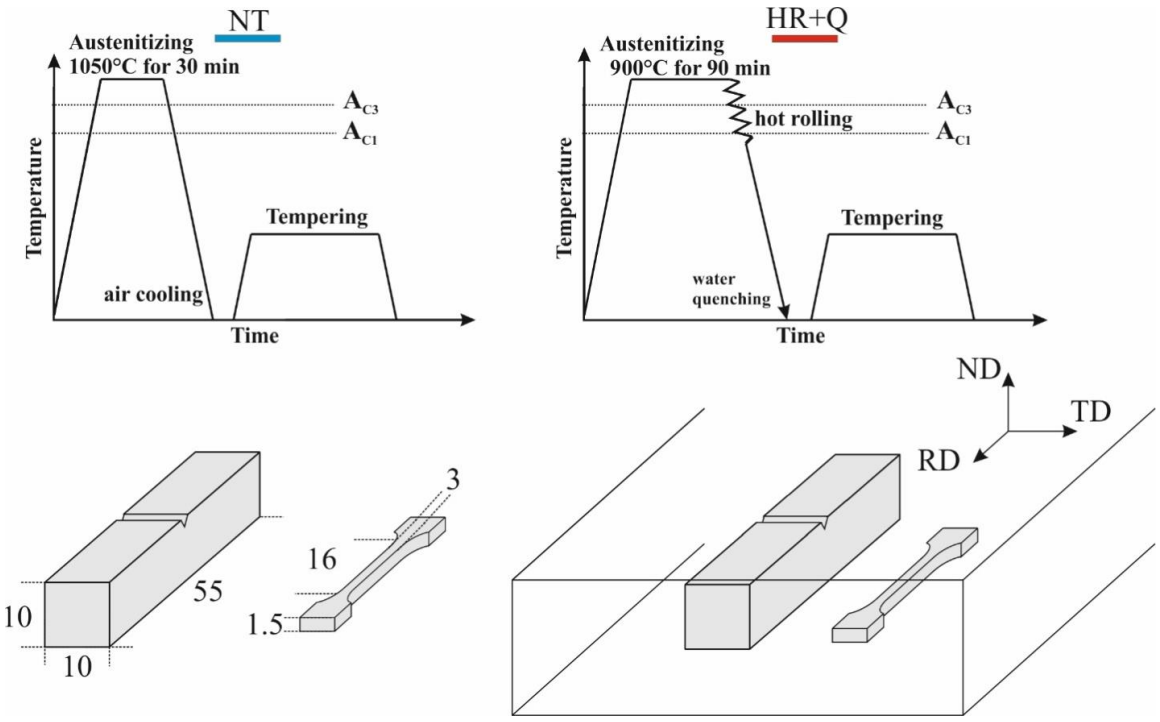

Figure 1. Schematic diagrams of thermal and thermo-mechanical heat treatments and schematic view of the rolled steel plate showing the orientation and dimensions of tensile and Charpy impact specimens (All dimensions are in mm).

The microstructures of the steel samples were analyzed by JEOL JEM-2100 transmission electron microscope (TEM) with an INCA energy-dispersive X-ray spectrometer (EDS) and a FEI Quanta 600 FEG and Nova NanoSEM 250 scanning electron microscopes (SEM) operated at 20 kV and equipped with EBSD analysis system. The samples for SEM observations and thin foils for TEM analysis were prepared using electrolytic polishing and double jet polishing techniques, respectively, using 10% $HClO_4$ solution in CH_3COOH. The density of the lattice dislocation on TEM micrographs was estimated by counting individual dislocations crossing the thin foil surfaces [33]:

$$\rho_{TEM} = \frac{N}{A}, \tag{1}$$

where N is the number of dislocations and A is the selected area.

The precipitate residues were extracted by electrolytically dissolving the matrix of the bulk samples using 5% HCl solution in C_2H_5OH at applied voltage of 20 V. At least 0.4 g of each sample was dissolved. The insoluble residues were separated by a centrifuge, using

a rotor speed of 4000 rpm for 10 min. The obtained residues were air dried and weighed. The total mass fraction of residues w_r in the steel samples was then calculated as:

$$w_r = \frac{m_r}{m_r + m_M}, \quad (2)$$

where m_r is the mass of the dried residue and m_M is the mass of the dissolved matrix. The equilibrium mass fractions of precipitates were calculated using the Thermo-Calc software package integrated with TCFE7 steel database.

3. Results

3.1. Tensile Properties

The dependences of the yield strength (YS), the ultimate tensile strength (UTS) and total elongation (TE) of the HR+Q and NT steel samples on tempering temperature are shown in Figure 2a. Both untempered HR+Q and NT samples are characterized by YS of about 1000 MPa and TE of 10%. UTS of the NT samples after tempering at T $\leq$ 500 °C is about 100 MPa higher than that of the steel in HR+Q condition. YS increases with increasing tempering temperature to T $\leq$ 500 °C and then decreases rapidly. With increasing tempering temperature from 500 to 780 °C, the difference in UTS of the HR+Q and NT samples gradually disappears. The stress–strain curves of the untempered steel samples and those tempered at 780 °C for 3 h are shown in Figure 2b. The steel samples exhibit continuous yielding behavior and TE generally increases after high temperature tempering. The observed values of YS and UTS for the NT and HR+Q samples after tempering at 750 °C are similar to those for a P92 steel (YS = 480 MPa, UTS = 700 MPa) tempered under the same conditions [34].

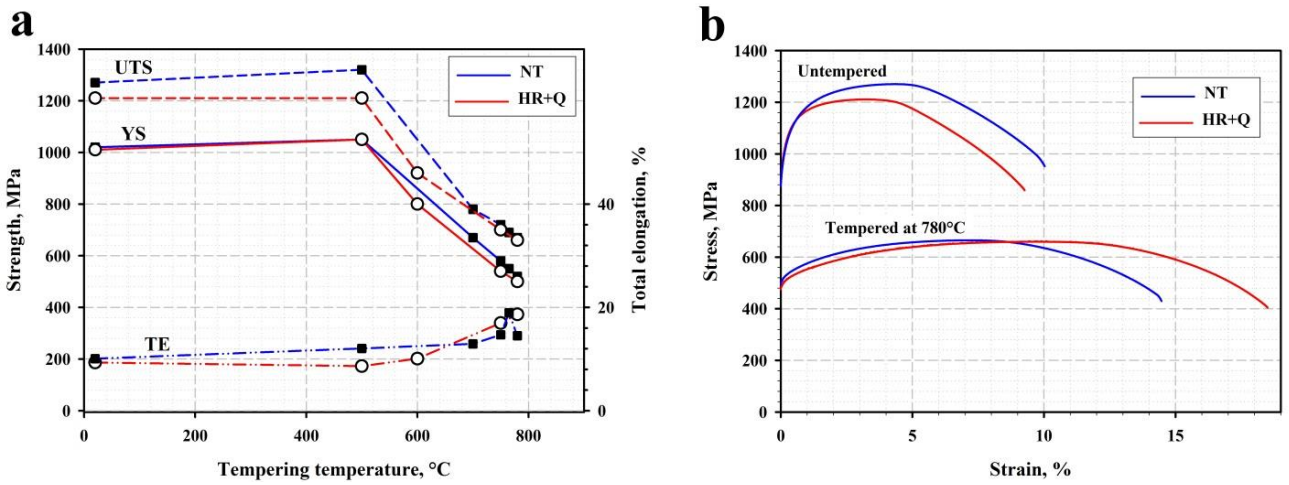

Figure 2. The effect of tempering temperature on the tensile properties of the NT and HR+Q samples (**a**) and the engineering stress–strain curves of the NT and HR+Q samples (**b**).

3.2. Impact Toughness and DBTT

The as-normalized steel shows an average impact toughness of 24 J/cm^2 that tends to decrease during subsequent tempering at temperatures below 500 °C (Figure 3a). The impact toughness of the NT samples tempered at 600–765 °C varies from 18 to 40 J/cm^2, indicating the prevalence of the brittle fracture of the steel in this condition. With increasing tempering temperature to 780 °C and 800 °C, the impact toughness increases to 135 J/cm^2 and 221 J/cm^2, respectively. In contrast to the NT condition, the untempered HR+Q sample shows a low toughness of 6 J/cm^2, and tempering at 500 °C has no effect on the impact behavior. The tempering at T $\geq$ 700 °C results in a remarkable improvement in the impact toughness of HR+Q samples.

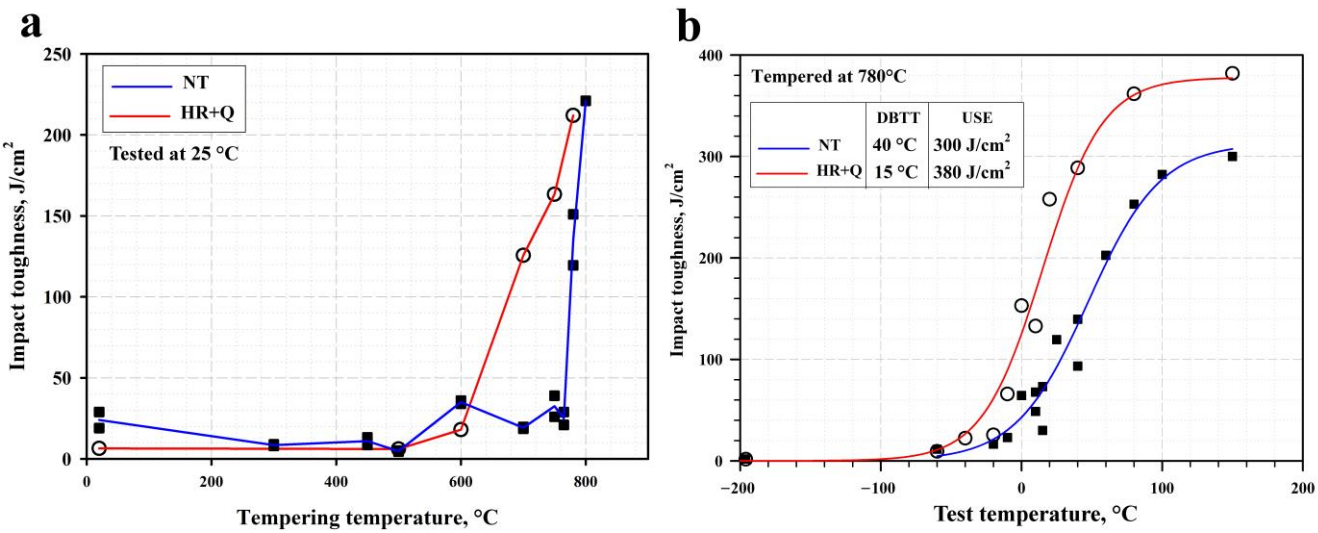

Figure 3. The effect of tempering temperature on the impact toughness of the NT and HR+Q samples (**a**) and the Charpy impact absorbed energy vs. impact test temperature curves of the NT and HR+Q samples tempered at 780 °C for 3 h (**b**).

The significant increase in the fracture toughness of the NT sample as observed after tempering at 780 °C correlates with the precipitation of Ta-rich MX carbonitrides, which are expected to have a significant effect on the creep strength [32]. Thus, the HR+Q and NT specimens were subjected to tempering at 780 °C and tested at various temperatures from −196 to 150 °C in order to determine the effect of hot-rolling on the fracture behavior. The obtained Charpy impact curves fitted by the Boltzmann function are depicted in Figure 3b. The steel after HR+Q possesses a lower DBTT (15 vs. 40 °C) and higher USE (380 vs. 300 J/cm^2) than that after NT treatment while the cryogenic impact toughness at −196 °C is about 2 J/cm^2 after both HR+Q and NT treatments.

3.3. Microstructure and Precipitate Analysis

Figure 4a,c shows the EBSD IPF (inverse pole figure) maps of the untempered NT and HR+Q samples. The boundary maps with misorientation angles of 22°–48° highlighting the prior γ grains are represented in Figure 4b,d. The microstructures in the samples are quite different. The lath martensite structure with relatively large size of prior austenite grains (PAG) of 46 ± 4 μm evolves in the steel after normalization at 1050 °C. Whereas, the coarse elongated PAGs with the mean size of 340 ± 50 μm were observed in the HR+Q sample, thus indicating the austenite deformation during rolling below austenite recrystallization temperature. The measured size of the martensite packets was 25 ± 3 μm and 83 ± 15 μm for the NT and HR+Q samples, respectively (Table 2). The <002> pole figure from the single prior austenite grain in the HR+Q sample is shown in Figure 4e. It is seen that child martensite obeys Kurdjumov–Sachs (K-S) orientation relationships (OR) of {111}A ‖ {101}M, <110> A‖ <111>M to the parent austenite phase, and all the 24 variants appear within PAGs. Almost random texture is expected in the NT sample. In contrast, the hot-rolled austenite affected the texture in HR+Q samples. Figure 4f shows the φ_2 = 45° section of the orientation distribution function (ODF) of the untempered HR+Q sample along with the various texture components. The major components of the texture of the untempered HR+Q sample are {332}<113> and {112}<111>. Slightly increased intensity is also observed for {001}⟨100⟩ Cube texture. The distributions of grain boundaries with different misorientation angles are shown in Figure 5. The low fraction of the boundaries with misorientations between 20° and 49° is a typical crystallographic feature of the martensite transformation [35]. The fraction of low-angle boundaries in the HR+Q sample is somewhat smaller than that in the NT sample. The substructure of

both untempered NT and HR+Q samples is lath martensite with high density of tangled dislocations of 10^{15} m^{-2} and carbide particles (Figure 6, Table 2).

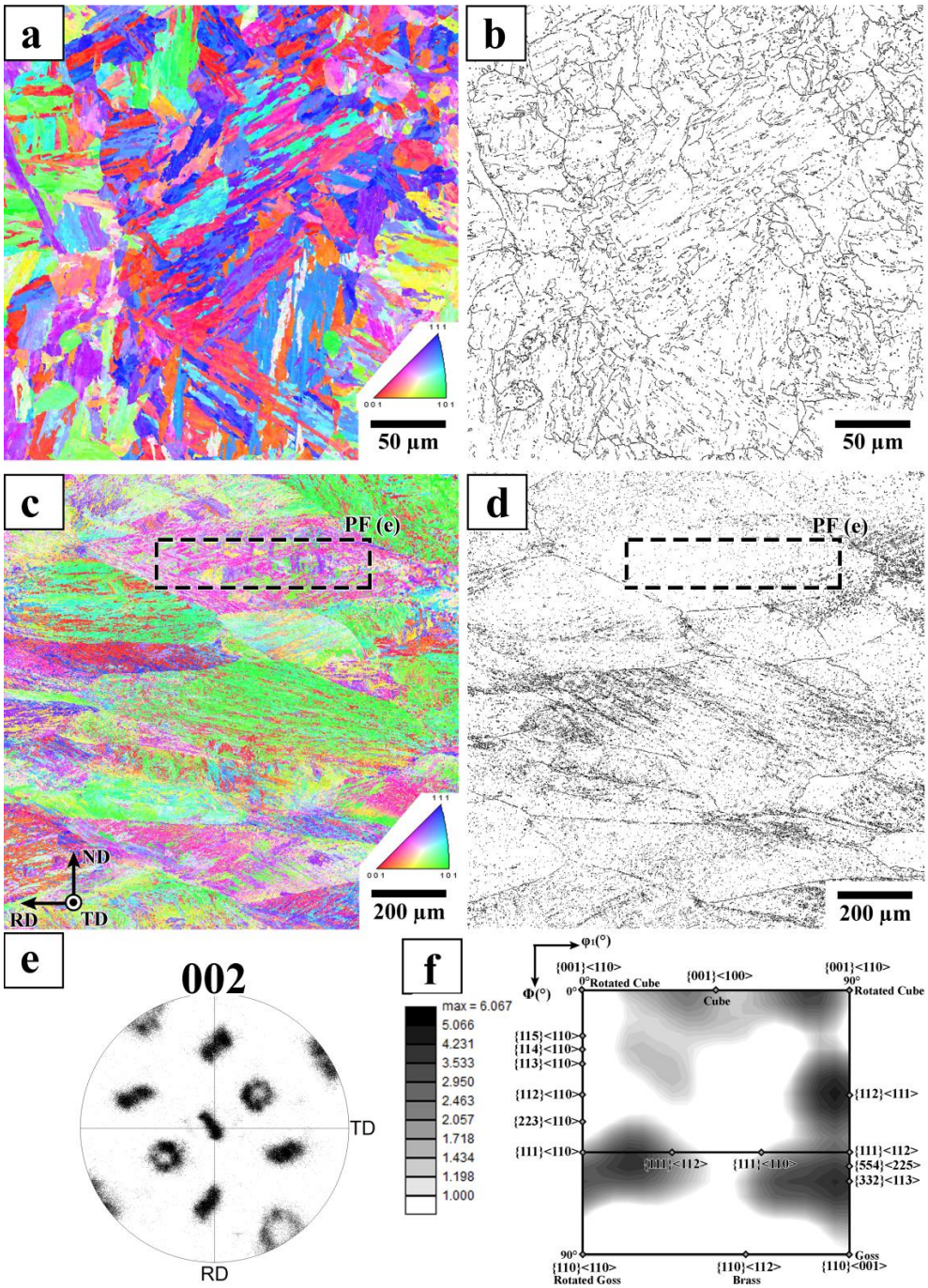

Figure 4. EBSD analysis of the untempered NT (**a**,**b**) and HR+Q (**c**–**f**) samples. Inverse pole figure maps for TD (**a**,**c**) and grain boundary maps showing the boundaries with misorientations between 20° and 49° to reveal PAGs (**b**,**d**). The <002> pole figure (**e**) and ODF (φ_2 = 45° section) of the HR+Q sample (**f**).

Table 2. Microstructural parameters and the mean size of precipitates in the NT and HR+Q samples.

Sample	State	PAG Size (OM), μm	Packet Size (EBSD), μm	Lath Thickness (TEM), μm	ρ_{TEM}, $m^{-2} \times 10^{14}$	Mean Length/Width of M_3C Carbide, nm	Mean Size of $M_{23}C_6$ carbide, nm	Mean Size of MX Carbonitrides, nm
NT	Untempered	46 ± 4	25 ± 3	0.19 ± 0.02	10.0 ± 4.3	80/11	-	38
	Tempered at 780 °C	-//-	-//-	0.36 ± 0.05	0.9 ± 0.3	-	79	21
HR+Q	Untempered	340 ± 50	83 ± 15	0.41 ± 0.06	9.8 ± 3.9	-	69	6
	Tempered at 780 °C	-//-	-//-	0.46 ± 0.05	0.5 ± 0.2	-	102	15

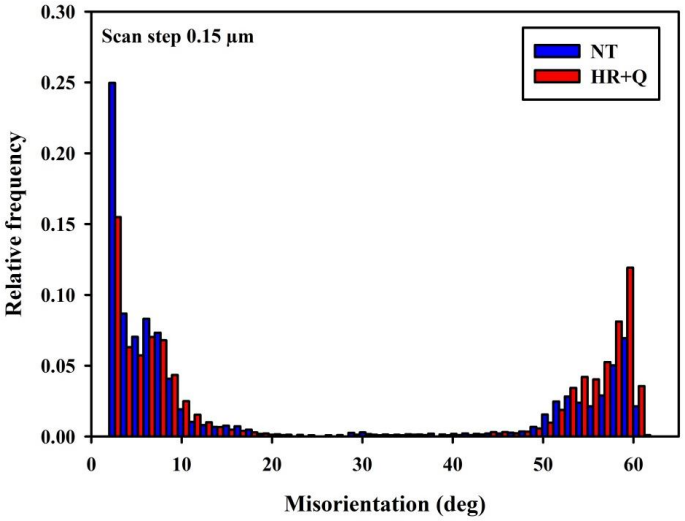

Figure 5. The distributions of grain boundary misorientations in the untempered NT and HR+Q samples.

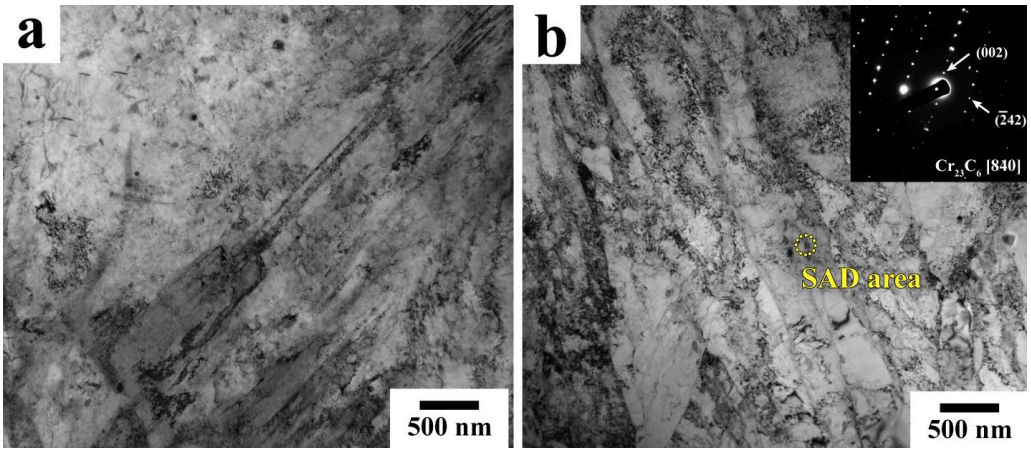

Figure 6. TEM images of lath martensite in the untempered NT (**a**) and HR+Q (**b**) samples.

It was previously shown that the steel normalized at 1050 °C contains the autotempered needle-like cementite particles and MX-type carbonitrides [32]. The mean width of martensite laths formed during HR+Q treatment is about two times larger than that formed during the NT treatment (0.40 μm vs. 0.19 μm). However, this difference diminishes after tempering at 780 °C.

The suppressed lath/subgrain boundary migration during tempering of the steel after HR+Q treatment may be due to the pinning effect from the thermodynamically stable carbide particles. The selected area diffraction (SAD) and EDX analysis of the secondary precipitates in the untempered HR+Q sample reveal the presence of $M_{23}C_6$ particles with sizes ranging between 30 and 240 nm. Additionally, the precipitation of

uniformly dispersed Ta-rich MX particles with the mean size of 15 nm was observed. These particles are primarily located on the dislocations in lath interiors as shown in Figure 7. It is worth noting that the mean size of the MX particles in the steel after thermo-mechanical treatment is notably smaller than that in the NT sample (Table 2). Moreover, the finer distribution of the MX carbonitrides maintains after subsequent tempering at 780 °C. The SEM images of the NT and HR+Q samples in both the untempered condition and tempered at 780 °C are given in Figure 8.

It is seen that $M_{23}C_6$ particles in the HR+Q sample are distributed more homogeneously than in the NT sample. Figure 9 shows the mass fraction of the extracted precipitate residue as function of tempering temperature along with thermodynamic-based calculations performed using Thermo-Calc. The mass fraction of the precipitates in the untempered HR+Q sample is ~65% higher than that of the steel after NT treatment.

Further tempering at a temperature above 500 °C is accompanied by an increase in the total amount of the precipitate residue towards to the thermodynamically stable value. Note that the equilibrium mass fraction of the secondary precipitates including $M_{23}C_6$ and MX phases is calculated to be 0.35% at 900 °C. Therefore, the presence of $M_{23}C_6$ particles in the as-quenched HR+Q treated steel can be justified by the lower austenitization temperature (900 °C) which lies below the solvus temperature of this precipitating phase. Thus, in contrast to conventional normalizing treatment, a certain proportion of the $M_{23}C_6$ particles is formed during the hot-rolling process and is maintained in the steel after subsequent water quenching.

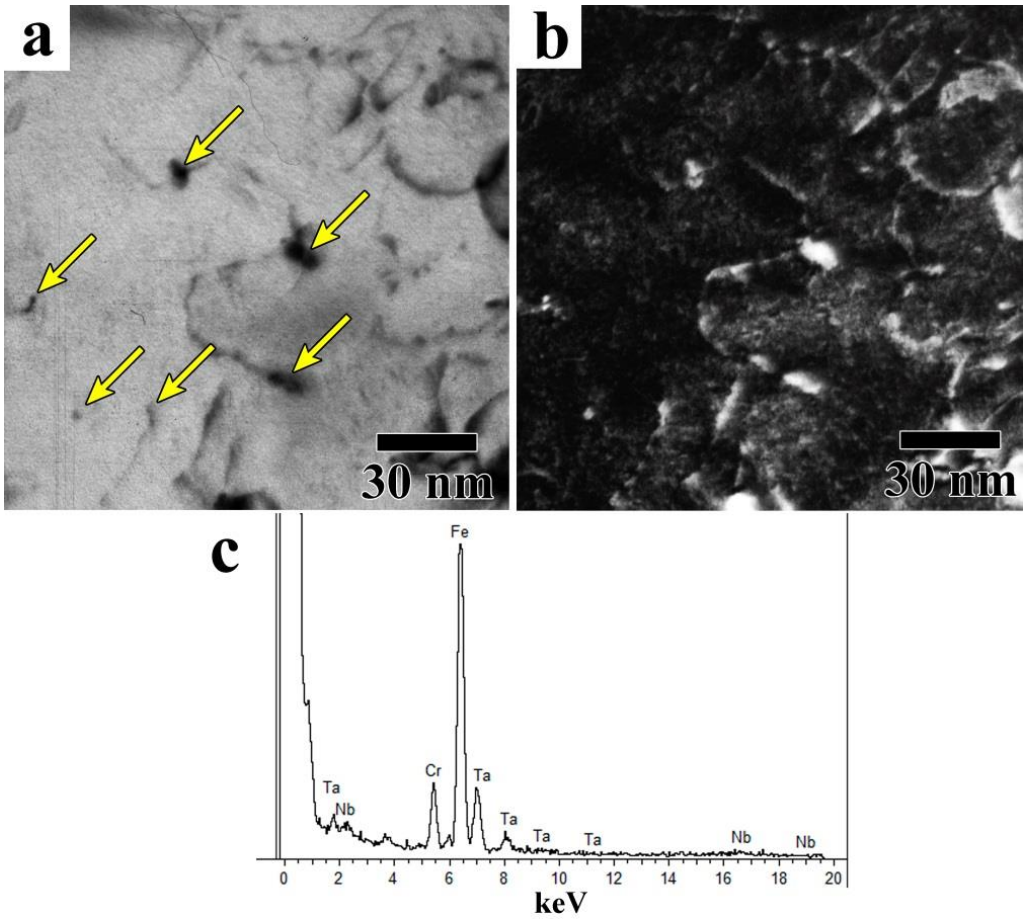

Figure 7. Bright-field (**a**) and dark-field (**b**) TEM images of the untempered HR+Q sample, illustrating the fine Ta-rich MX particles (highlighted by yellow arrows in (**a**)) precipitated on the dislocations with the corresponding EDS spectra (**c**).

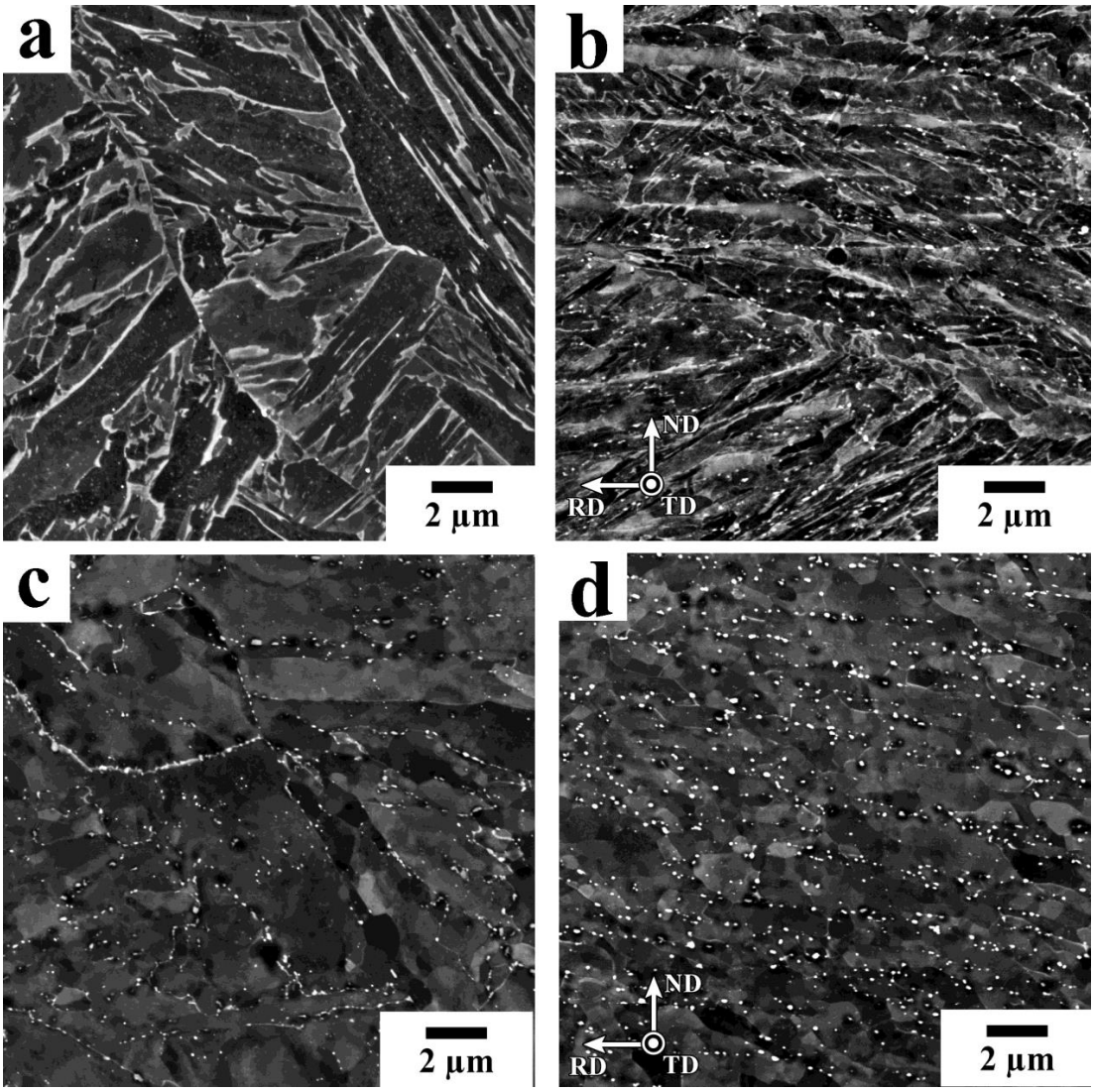

Figure 8. SEM micrographs of the NT (**a**,**c**) and HR+Q (**b**,**d**) samples in the untempered condition (**a**,**b**) and tempered at 780 °C (**c**,**d**).

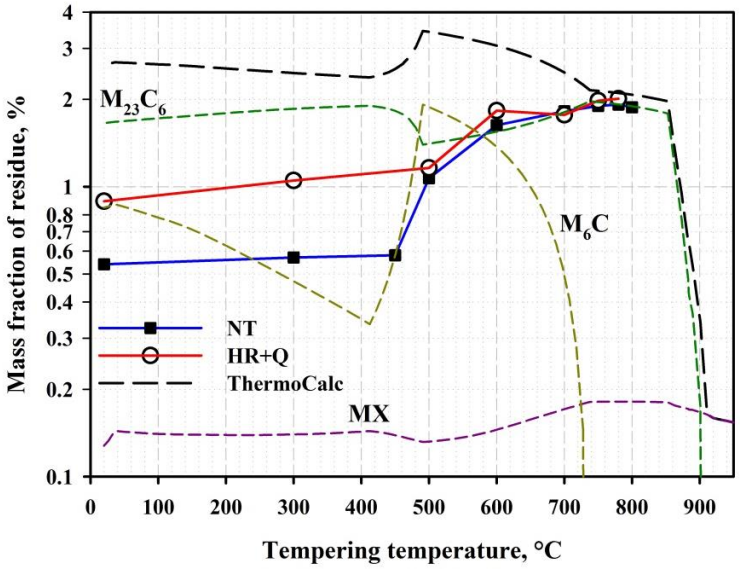

Figure 9. Mass fractions of the extracted precipitate residues as a function of tempering temperature.

4. Discussion

The microstructural changes have a significant influence on the impact absorbed energy. To examine the relationship between the microstructure and the fracture behavior, the impact load versus displacement curves obtained during instrumented Charpy impact tests are considered below. The total absorbed impact energy is composed of the crack initiation energy, Wi, the crack propagation energy, Wp, and the crack arrest energy, Wa [36,37]. The obtained values of the absorbed energy and the maximum load (P_M) for the steel in different conditions are summarized in Table 3. To evaluate the dynamic ultimate tensile strength (σ_{UTSd}), the following experimental relationship was used [38]:

$$\sigma_{UTSd} = \frac{2.385 P_M W}{(W-a)^2 B}, \quad (3)$$

where W is the specimen width (10 mm), B is the specimen thickness (10 mm) and a is the notch depth (2 mm).

Table 3. Impact toughness, the energies absorbed at different crack propagation stages and dynamic parameters calculated from load–deflection curves.

Sample	State	Impact Toughness, J/cm^2	Crack Initiation Energy (Wi), J	Crack Propagation Energy (Wp), J	Crack Arrest Energy (Wa), J	P_M, kN	σ_{UTSd}, MPa
NT	Untempered	24	13.7	5.5	-	29.3	1080
	Tempered at 500 °C	5	1.8	1.7	-	6.8	255
	Tempered at 700 °C	19	3.4	8.3	3.2	12.5	465
	Tempered at 780 °C	96	47.4	12.2	17.1	21.8	810
HR+Q	Untempered	6	3.5	1.7	-	11.1	410
	Tempered at 500 °C	6	2.1	3.0	-	7.0	260
	Tempered at 700 °C	125	11.4	84.8	4.3	21.3	795
	Tempered at 780 °C	212	50.3	96.0	23.2	20.3	755

The dynamic ultimate tensile strengths of the NT sample tempered at 500–700 °C and the HR+Q sample tempered at T $\leq$ 500 °C are significantly lower than UTS values obtained during tensile tests. This suggests that the crack initiates without plastic deformation that is typical for the brittle fracture mechanism. The SEM fractography of the fractured steel samples tempered at 500 °C reveals the quasi-cleavage facets with a river pattern (Figure 10). The size of the facets in the HR+Q sample are slightly larger than those in the NT sample, which correlates with the difference in the sizes of PAGs and packets (Table 2), similar to the observations of Schino et al. [39]. The most common mechanism of the cleavage fracture initiation in steels involves the cracking of the inclusions or second phase particles due to plastic strain in the surrounding matrix [40–42]. Thus, the large packets and the presence of relatively coarse $M_{23}C_6$ particles in the untempered HR+Q sample facilitates the crack initiation and propagation. As a result, the fracture occurs at a lower applied load and is characterized by low adsorbed energy as compared to that for the NT sample in the untempered condition (Table 3).

The effect of the microstructure on the brittle fracture was also analyzed by observing the secondary microcrack on the cross section close to the fracture surface of the ruptured NT sample tempered at 500 °C (Figure 11). The observed crack has a length of ~20 µm and is oriented at an angle of 30° to the primary crack propagation direction. The IPF map and corresponding <002> pole figure clearly indicate that the crack is located within the single PAG. Further consideration of the martensite variants show that the crack mostly propagated along the {001} cleavage planes across the V1/V4 sub-blocks pair of the KS OR. The stepwise crack path suggests that the crack propagated in a discontinuous manner. The traced image of the fracture surface together with the block and packet boundaries of the lath martensite reveal that the deflections of the crack path are associated with the change in the crystal orientation between the different martensite packets and sub-block

pairs. As the misorientation between sub-blocks is approximately 10° and that between laths is 1–5° [35], it can be concluded that the boundaries between these microstructural units are not effective in cleavage crack deflection, and thus cannot be treated in terms of the effective grain size. In contrast, the high-angle boundaries of blocks and packets have a similar ability to impede crack growth, which is in good agreement with other studies of fracture behavior of lath martensite in low-alloy steels [43–45].

Since a significant difference in the impact behavior is found for the NT and HR+Q specimens fractured at room temperature after tempering at 700 °C, the load–deflection curves and fracture morphology are examined in this state (Figure 12).

The onset of the rapid crack propagation occurs immediately after peak load in both NT and HR+Q samples. However, the remarkable difference in the slope of the load–deflection curve at this stage is linked to the change in the fracture mode. The brittle fracture in the crack propagation zone of the NT sample is characterized by transgranular cleavage facets, while the fractured surface of the HR+Q specimen is composed of cleavage facets separated by ductile dimples and tear ridges. The substantial post-peak load energy absorption correlates with the large shear lip zones in the HR+Q sample. Moreover, the presence of numerous large secondary cracks is linked to the delamination effect, which is also confirmed by the load drops on the load–deflection curve (marked by the black arrows in Figure 12). The presence of delamination was often observed in the hot-rolled martensitic steels and associated with the development of crystallographic texture [30,46]. In these steels the texture of the deformed parent γ grains is inherited by martensite during the transformation. The major transformation textures inherited by α from γ are $\{332\}\langle 113\rangle$; $\{113\}\langle 110\rangle$ and $\{100\}\langle 011\rangle$ [28]. The crystallographic textures affect the impact toughness by changing the densities of $\{001\}$ cleavage planes lying parallel to the fracture surface of impact specimens. The $\{332\}\langle 113\rangle$ component is the most desirable among the transformation textures of the hot-rolled steels due to good formability, strength and impact toughness [28,30]. Figure 13 represents the intensity of the major texture components in the HR+Q sample. In this sample, the $\{332\}\langle 113\rangle$ texture has the highest intensity among the observed texture components. This texture originates from the copper $\{112\}\langle 111\rangle$ component of deformed austenite [28]. The $\{001\}\langle 110\rangle$ component usually originated from the Cube $\{001\}\langle 100\rangle$ component of the recrystallized austenite and has a low intensity in the studied steel; thus, it has a little effect on the fracture behavior.

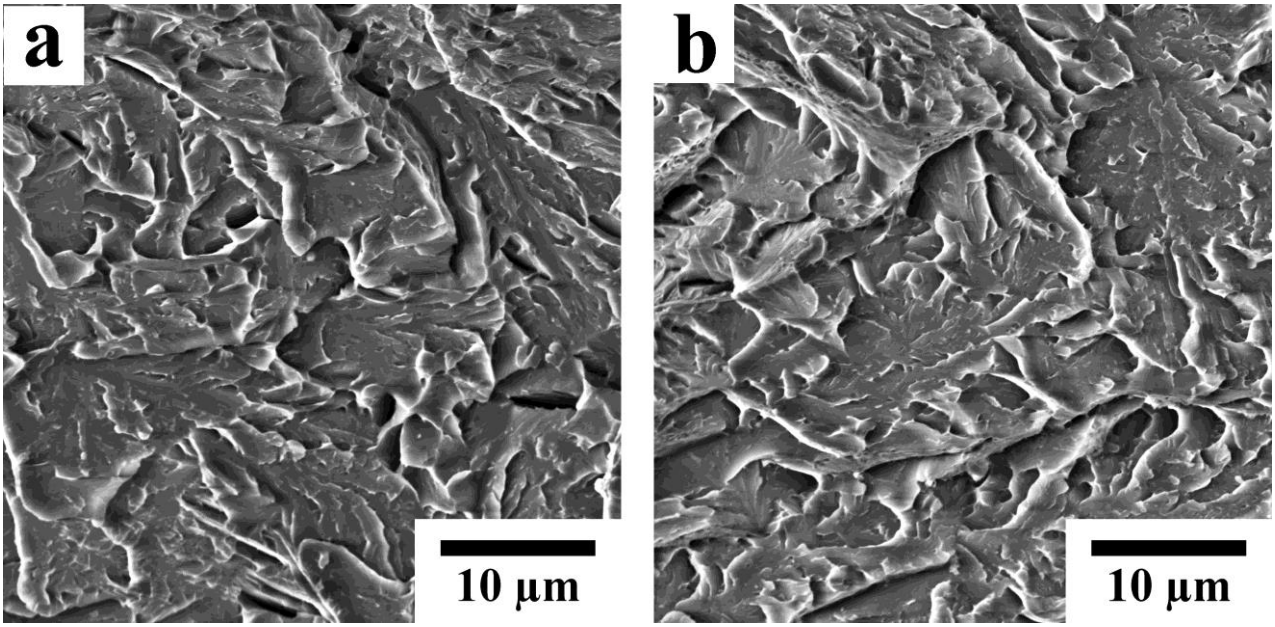

Figure 10. SEM images showing the fracture surface of the NT (**a**) and HR+Q (**b**) samples tempered at 500 °C.

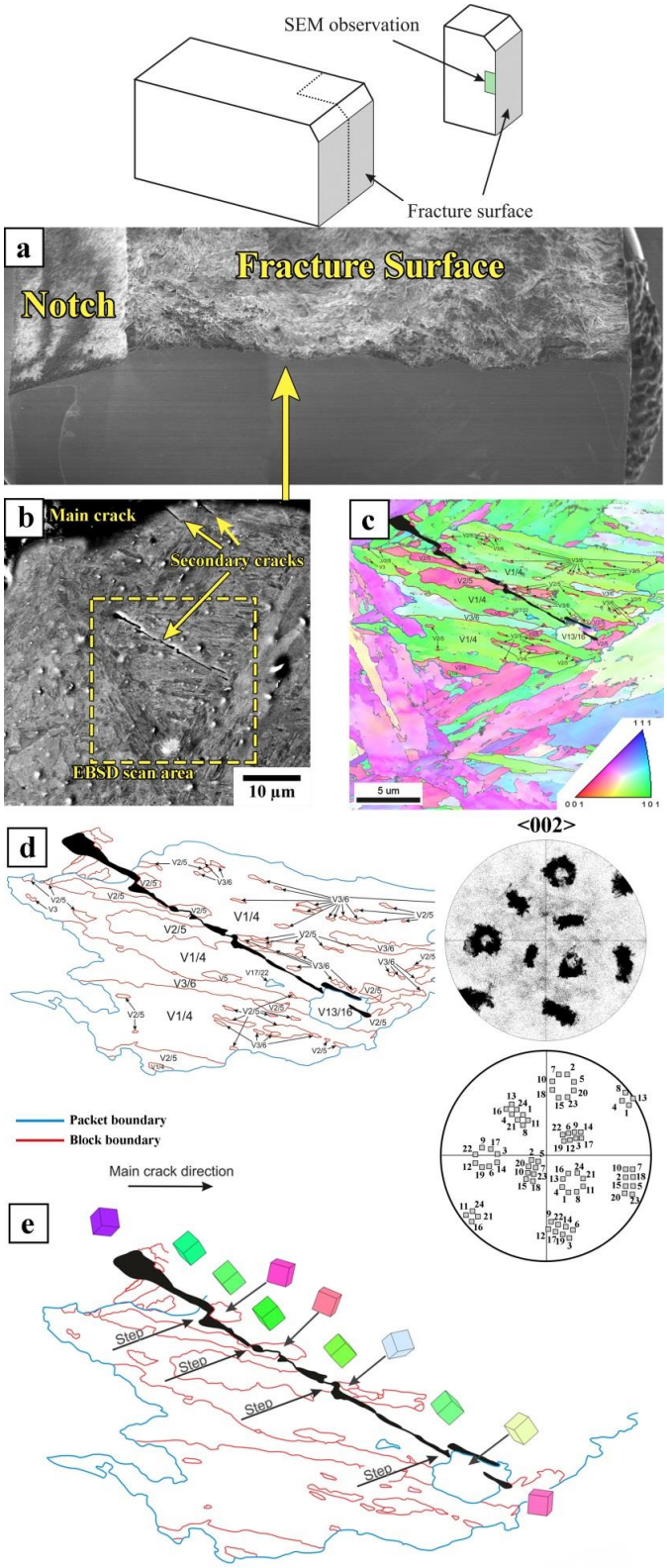

Figure 11. SEM analysis of the secondary crack propagation in the NT sample tempered at 500 °C: schematic and overall view of the ruptured Charpy specimen (**a**); SEM cross section image revealing secondary cracks near to fracture surface (**b**); IPF map of the selected EBSD scan area (**c**); the variant analysis of the lath martensite structure along the observed secondary crack and theoretical <002> pole figure of martensite variants inside an austenite grain satisfying the K-S OR (**d**); the grain boundary map showing the appearance of the crack deflection and corresponding three-dimensional crystal orientations represented by unit cell cubes at the fracture surface (**e**).

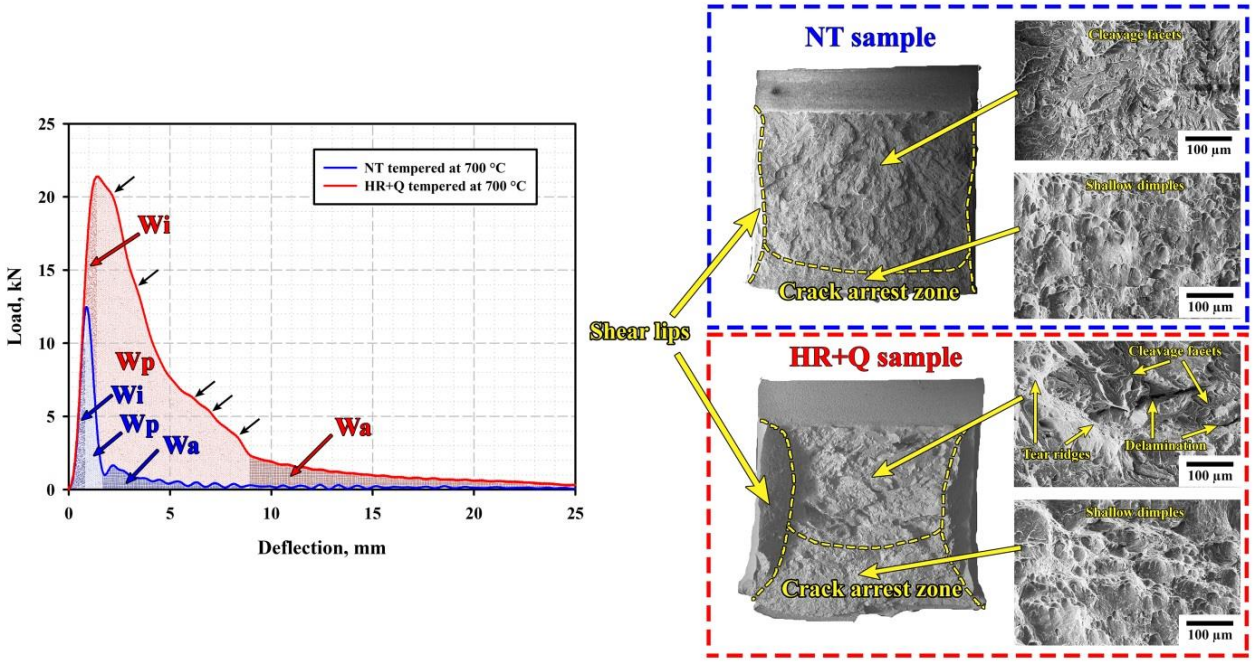

Figure 12. Load–deflection curves obtained during impact tests of the NT and HR+Q specimens tempered at 780 °C and the corresponding SEM images of the fracture surfaces.

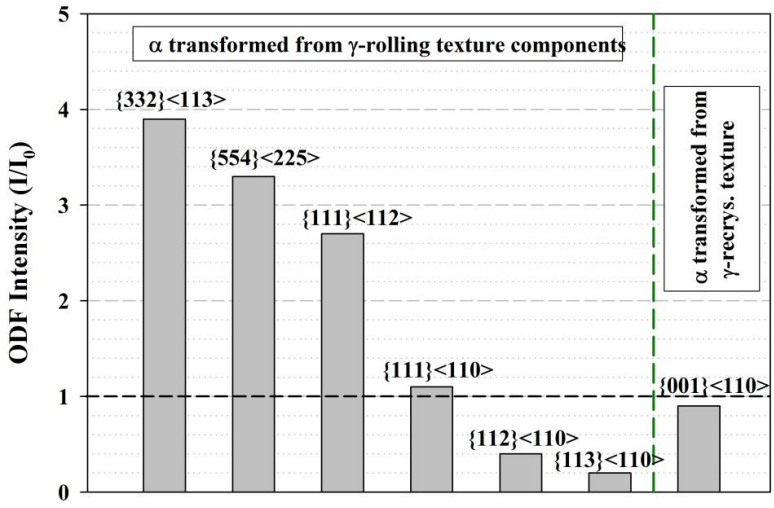

Figure 13. Major texture components in the untempered HR+Q sample.

An increased USE value of the tempered HR+Q steel sample is also indicating the enhanced energy consumption of the ductile fracture as compared to that in the tempered NT sample. The pronounced crack propagation stage on the load–deflection curves of the HR+Q samples tempered at 780 °C and tested at 20 and 150 °C suggests a relatively slow crack growth rate (Figure 14).

Figure 15 illustrates the fracture surface morphology of the steel samples tempered at 780 °C and tested at 150 °C. The dimple pattern produced by ductile tearing in the NT sample is characterized by a large number of small dimples, whereas the long and narrow dimples mixed with small round dimples appeared on the tear ridges in the HR+Q sample. The ductile crack propagation involves the nucleation, growth and coalescence of microvoids. The microvoids are formed around the second phase particles when sufficient stress is applied [41,47]. This is well agreed with in the SEM observations of the second phase particles inside the dimples (Figure 15).

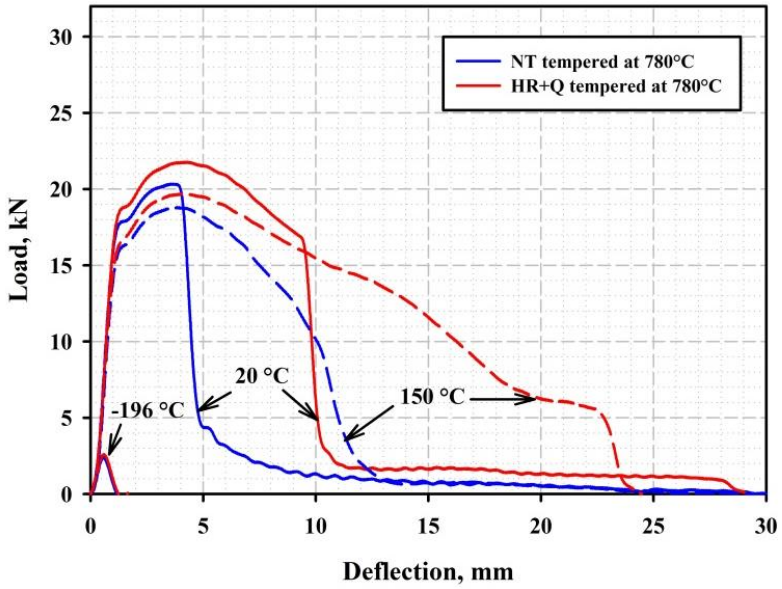

Figure 14. Load–deflection curves of the NT and HR+Q samples tempered at 780 °C and tested at −196, 20 and 150 °C.

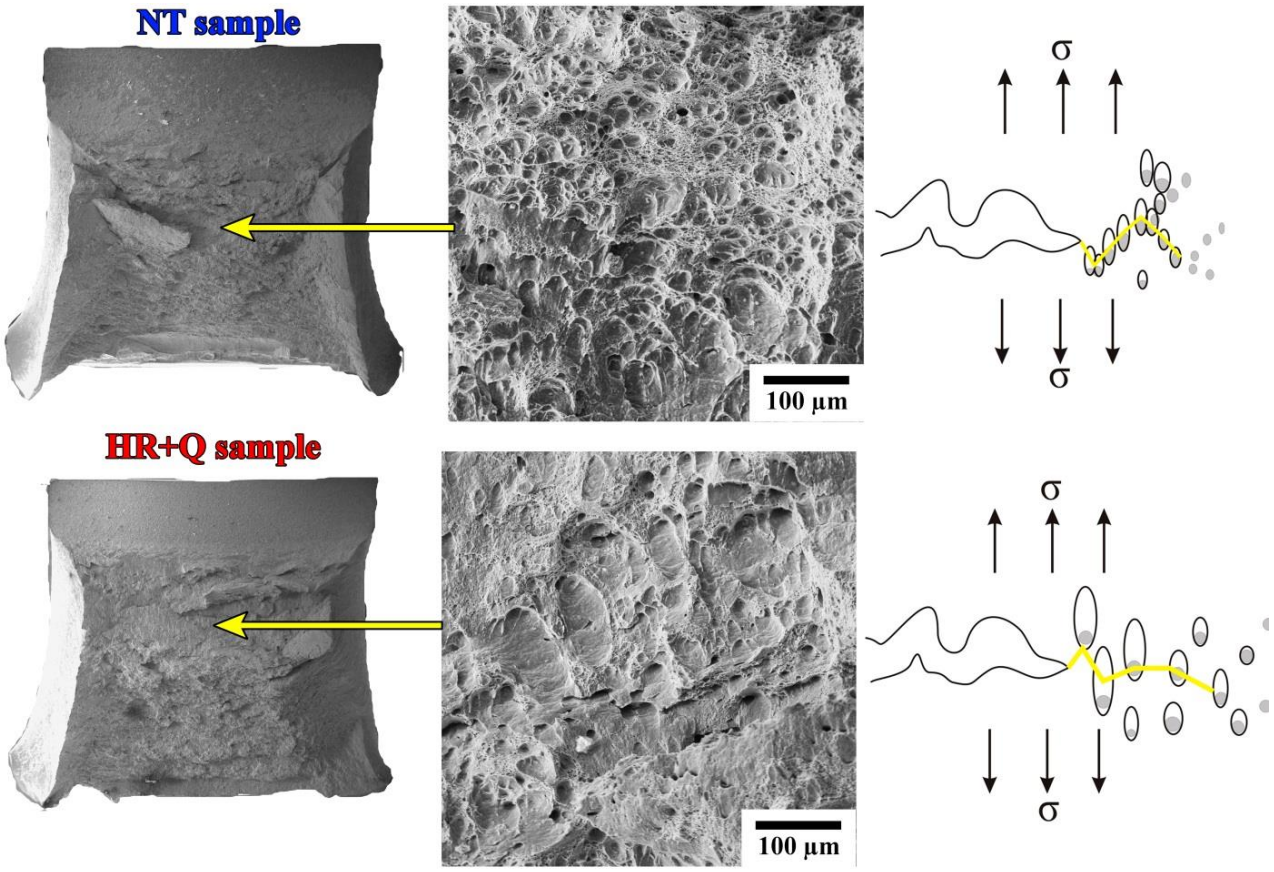

Figure 15. SEM images showing the fracture surface of the NT and HR+Q samples tempered at 780 °C and tested at 150 °C along with schematic illustration of the ductile crack propagation process.

It can be assumed that each formed void grows independently until it merges with neighboring voids. Therefore, the local distribution of the precipitates plays an important role in a ductile fracture. The preferred precipitation of the $M_{23}C_6$ carbides on the boundaries of PAGs, packets and blocks is an inherent feature of the tempered lath martensite

structure [1,37,48,49]. In this structure the grain boundary precipitates are located closely to each other, and the formed chains of particles act as the favorable path for the crack growth. Since the carbide particles in the tempered NT sample are closely spaced, instability occurs soon after these smaller voids form, resulting in the fine dimple pattern on the fracture surface. In contrast, in the microstructure with uniformly distributed particles, the ductile fracture is accompanied by a considerable plastic deformation in the formed voids followed by the void linkage. As a consequence, the HR+Q sample tempered at 780 °C shows higher crack propagation energy compared to the tempered NT sample. The uniform distribution of the $M_{23}C_6$ precipitates and increased density of MX nanoprecipitates after HR+Q treatment is also expected to be beneficial for the creep resistance of the studied steel.

5. Conclusions

1. Hot-rolling of 9%Cr steel in the range of metastable γ-phase at 900–700 °C followed by water quenching and tempering at T ≥ 700 °C results in a better impact toughness compared to conventional normalization and tempering heat treatment. After tempering at 780 °C, the HR+Q specimens exhibited a lower DBTT (15 vs. 40 °C) and higher upper shelf energy (380 vs. 300 J/cm^2) than the NT specimens. The presence of numerous large secondary cracks on the fracture surface of the ruptured HR+Q samples is associated with the delamination effect.
2. The hot-rolled and quenched steel is characterized by the lath martensite structure with relatively large elongated PAGs of 340 ± 50 μm. Two types of precipitates are observed in this condition. The dispersed particles of $M_{23}C_6$ carbide with the mean size of 69 nm are uniformly dispersed on the lath/subgrain boundaries, whereas fine Ta-rich MX carbonitride particles with a size of ~6 nm are precipitated on the dislocations. Further tempering is accompanied by a decrease in the dislocation density and an increase in the total amount of precipitates towards the equilibrium content. Nevertheless, the mean size of MX carbonitride particles after tempering at 780 °C (15 nm) is still significantly smaller than that in the NT sample (21 nm).
3. The brittle fracture in the studied steel occurs via crack propagation along the {001} cleavage planes. The high-angle boundaries of martensite packets and blocks hinder the crack propagation while low-angle sub-block and lath boundaries are ineffective in retarding the cleavage crack propagation. The increased impact toughness of the tempered HR+Q steel sample is attributed to the favorable {332}⟨113⟩ crystallographic texture and considerable plastic deformation during ductile fracture in the microstructure with uniformly distributed particles.

Author Contributions: Conceptualization, E.T., A.B. and R.K.; methodology, E.T.; formal analysis, E.T.; investigation, E.T.; data curation, E.T. and A.B.; writing—original draft, E.T.; writing—review and editing, E.T. and A.B.; visualization, E.T.; supervision, A.B. and R.K. All authors have read and agreed to the published version of the manuscript.

Funding: This research was funded by Russian Science Foundation grant number 21–79-00067.

Data Availability Statement: Data will be made available on request.

Acknowledgments: The work was carried out using the equipment of the Joint Research Center, "Technology and Materials", of Belgorod State National Research University.

Conflicts of Interest: The authors declare no conflict of interest.

References

1. Abe, F.; Horiuchi, T.; Taneike, M.; Sawada, K. Stabilization of Martensitic Microstructure in Advanced 9Cr Steel during Creep at High Temperature. *Mater. Sci. Eng. A* **2004**, *378*, 299–303. [CrossRef]
2. Di Schino, A.; Gaggiotti, M.; Testani, C. Heat Treatment Effect on Microstructure Evolution in a 7% Cr Steel for Forging. *Metals* **2020**, *10*, 808. [CrossRef]
3. Onizawa, T.; Wakai, T.; Ando, M.; Aoto, K. Effect of V and Nb on Precipitation Behavior and Mechanical Properties of High Cr Steel. *Nucl. Eng. Des.* **2008**, *238*, 408–416. [CrossRef]

4. Matsunaga, T.; Hongo, H.; Tabuchi, M.; Souissi, M.; Sahara, R.; Whitt, C.; Zhang, W.; Mills, M.J. Creep Lifetime and Microstructure Evolution in Boron-Added 9Cr–1Mo Heat-Resistant Steel. *Mater. Sci. Eng. A* **2019**, *760*, 267–276. [CrossRef]
5. Semba, H.; Abe, F. Alloy Design and Creep Strength of Advanced 9%Cr USC Boiler Steels Containing High Concentration of Boron. *Energy Mater.* **2006**, *1*, 238–244. [CrossRef]
6. Dudova, N. 9–12% Cr Heat-Resistant Martensitic Steels with Increased Boron and Decreased Nitrogen Contents. *Metals* **2022**, *12*, 1119. [CrossRef]
7. Fedoseeva, A.; Tkachev, E.; Dudko, V.; Dudova, N.; Kaibyshev, R. Effect of Alloying on Interfacial Energy of Precipitation/Matrix in High-Chromium Martensitic Steels. *J. Mater. Sci.* **2017**, *52*, 4197–4209. [CrossRef]
8. Li, X.; Li, K.; Cai, Z.; Pan, J. A Review of Austenite Memory Effect in HAZ of B Containing 9% Cr Martensitic Heat Resistant Steel. *Metals* **2019**, *9*, 1233. [CrossRef]
9. Fedoseeva, A.; Tkachev, E.; Kaibyshev, R. Advanced Heat-Resistant Martensitic Steels: Long-Term Creep Deformation and Fracture Mechanisms. *Mater. Sci. Eng. A* **2023**, *862*, 144438. [CrossRef]
10. Tkachev, E.; Belyakov, A.; Kaibyshev, R. Creep Behavior and Microstructural Evolution of a 9%Cr Steel with High B and Low N Contents. *Mater. Sci. Eng. A* **2018**, *725*, 228–241. [CrossRef]
11. Sahara, R.; Matsunaga, T.; Hongo, H.; Tabuchi, M. Theoretical Investigation of Stabilizing Mechanism by Boron in Body-Centered Cubic Iron Through (Fe,Cr)23(C,B)6 Precipitates. *Metall. Mater. Trans. A Phys. Metall. Mater. Sci.* **2016**, *47*, 2487–2497. [CrossRef]
12. Sakuraya, K.; Okada, H.; Abe, F. BN Type Inclusions Formed in High Cr Ferritic Heat Resistant Steel. *Tetsu-To-Hagane.* **2004**, *90*, 819–826. [CrossRef]
13. Tkachev, E.; Belyakov, A.; Kaibyshev, R. Creep Strength Breakdown and Microstructure in a 9%Cr Steel with High B and Low N Contents. *Mater. Sci. Eng. A* **2020**, *772*, 138821. [CrossRef]
14. Yan, P.; Liu, Z.; Bao, H.; Weng, Y.; Liu, W. Effect of Tempering Temperature on the Toughness of 9Cr-3W-3Co Martensitic Heat Resistant Steel. *Mater. Des.* **2014**, *54*, 874–879. [CrossRef]
15. Mishnev, R.; Dudova, N.; Kaibyshev, R.; Belyakov, A. On the Fracture Behavior of a Creep Resistant 10% Cr Steel with High Boron and Low Nitrogen Contents at Low Temperatures. *Materials* **2020**, *13*, 3. [CrossRef] [PubMed]
16. Mishnev, R.; Dudova, N.; Dudko, V.; Kaibyshev, R. Impact Toughness of a 10% Cr Steel with High Boron and Low Nitrogen Contents. *Mater. Sci. Eng. A* **2018**, *730*, 1–9. [CrossRef]
17. Fedoseeva, A.; Nikitin, I.; Dudova, N.; Hald, J.; Kaibyshev, R. Effect of the Thermo-Mechanical Processing on the Impact Toughness of a 12% Cr Martensitic Steel with Co, Cu, W, Mo and Ta Doping. *Metals* **2022**, *12*, 3. [CrossRef]
18. Tkachev, E.; Belyakov, A. Effect of Tempering on Microstructure and Mechanical Properties of a Ta-Added 9%Cr Steel with High B and Low N Contents. *Proc. IOP Conf. Ser. Mater. Sci. Eng.* **2019**, *525*, 012049. [CrossRef]
19. Saini, N.; Pandey, C.; Mahapatra, M.M.; Narang, H.K.; Mulik, R.S.; Kumar, P. A Comparative Study of Ductile-Brittle Transition Behavior and Fractography of P91 and P92 Steel. *Eng. Fail. Anal.* **2017**, *81*, 245–253. [CrossRef]
20. Anil Kumar, P.; Vanaja, J.; Prasad Reddy, G.V.; Nageswara Rao, G.V.S. Effect of Thermomechanical Treatment and Tempering Temperature on Microstructure and Tensile Properties of India Specific Reduced Activation Ferritic Martensitic Steel. *J. Nucl. Mater.* **2023**, *574*, 154186. [CrossRef]
21. Mancini, S.; Langellotto, L.; Di Nunzio, P.E.; Zitelli, C.; Di Schino, A. Defect Reduction and Quality Optimization by Modeling Plastic Deformation and Metallurgical Evolution in Ferritic Stainless Steels. *Metals* **2020**, *10*, 186. [CrossRef]
22. Fedoseeva, A.; Kaibyshev, R. Impact Toughness of a 12% Cr Martensitic Steel: Conventional Heat Treatment vs. Thermo-Mechanical Processing. *Mater. Lett.* **2023**, *334*, 133754. [CrossRef]
23. Karthikeyan, T.; Dash, M.K.; Mythili, R.; Selvi, S.P.; Moitra, A.; Saroja, S. Effect of Prior-Austenite Grain Refinement on Microstructure, Mechanical Properties and Thermal Embrittlement of 9Cr-1Mo-0.1C Steel. *J. Nucl. Mater.* **2017**, *494*, 260–277. [CrossRef]
24. Chatterjee, A.; Chakrabarti, D.; Moitra, A.; Mitra, R.; Bhaduri, A.K. Effect of Deformation Temperature on the Ductile-Brittle Transition Behavior of a Modified 9Cr-1Mo Steel. *Mater. Sci. Eng. A* **2015**, *630*, 58–70. [CrossRef]
25. Prakash, P.; Vanaja, J.; Reddy, G.V.P.; Laha, K.; Rao, G.V.S.N. On the Effect of Thermo-Mechanical Treatment on Creep Deformation and Rupture Behaviour of a Reduced Activation Ferritic-Martensitic Steel. *J. Nucl. Mater.* **2019**, *520*, 65–77. [CrossRef]
26. Vivas, J.; Capdevila, C.; Jimenez, J.A.; Benito-Alfonso, M.; San-Martin, D. Effect of Ausforming Temperature on the Microstructure of G91 Steel. *Metals* **2017**, *7*, 236. [CrossRef]
27. Yin, S.; Liu, Y.; Zhao, F. Effect of Thermomechanical Treatment on MX Phase Precipitation Behavior in CLAM Steel. *Fusion Eng. Des.* **2021**, *173*, 112785. [CrossRef]
28. Jonas, J.J.; Butron-Guillen, M.P.; Savoie, J. Transformation Textures in Steels. *ISIJ Int.* **1994**, *34*, 927–942. [CrossRef]
29. Ghosh, A.; Kundu, S.; Chakrabarti, D. Effect of Crystallographic Texture on the Cleavage Fracture Mechanism and Effective Grain Size of Ferritic Steel. *Scr. Mater.* **2014**, *81*, 8–11. [CrossRef]
30. Yang, X.L.; Xu, Y.B.; Tan, X.D.; Wu, D. Relationships among Crystallographic Texture, Fracture Behavior and Charpy Impact Toughness in API X100 Pipeline Steel. *Mater. Sci. Eng. A* **2015**, *641*, 96–106. [CrossRef]
31. Chatterjee, A.; Dutta, A.; Sk, M.B.; Mitra, R.; Bhaduri, A.K.; Chakrabarti, D. Effect of Microalloy Precipitates on the Microstructure and Texture of Hot-Deformed Modified 9Cr-1Mo Steel. *Metall. Mater. Trans. A Phys. Metall. Mater. Sci.* **2017**, *48*, 2410–2424. [CrossRef]

32. Tkachev, E.; Kaibyshev, R. Effect of Tempering on the Precipitation Behavior of a Ta-Alloyed 9%Cr Steel with High B and Low N Contents. *Mater. Today Commun.* **2022**, *32*, 103938. [CrossRef]
33. Hirsch, P.B.; Howie, A.; Nicholson, R.B.; Pashley, D.W.; Whelan, M.J.; Marton, L. Electron Microscopy of Thin Crystals. *Phys. Today* **1966**, *19*, 93–95. [CrossRef]
34. Dudko, V.; Fedoseeva, A.; Kaibyshev, R. Ductile-Brittle Transition in a 9% Cr Heat-Resistant Steel. *Mater. Sci. Eng. A* **2017**, *682*, 73–84. [CrossRef]
35. Morito, S.; Tanaka, H.; Konishi, R.; Furuhara, T.; Maki, T. The Morphology and Crystallography of Lath Martensite in Fe-C Alloys. *Acta Mater.* **2003**, *51*, 1789–1799. [CrossRef]
36. Kang, J.; Wang, C.; Wang, G.D. Microstructural Characteristics and Impact Fracture Behavior of a High-Strength Low-Alloy Steel Treated by Intercritical Heat Treatment. *Mater. Sci. Eng. A* **2012**, *553*, 96–104. [CrossRef]
37. Fedorova, I.; Kostka, A.; Tkachev, E.; Belyakov, A.; Kaibyshev, R. Tempering Behavior of a Low Nitrogen Boron-Added 9%Cr Steel. *Mater. Sci. Eng. A* **2016**, *662*, 443–455. [CrossRef]
38. Lucon, E. Estimating Dynamic Ultimate Tensile Strength from Instrumented Charpy Data. *Mater. Des.* **2016**, *97*, 437–443. [CrossRef]
39. Di Schino, A.; Guarnaschelli, C. Effect of Microstructure on Cleavage Resistance of High-Strength Quenched and Tempered Steels. *Mater. Lett.* **2009**, *63*, 1968–1972. [CrossRef]
40. McMahon, C.J.; Cohen, M. Initiation of Cleavage in Polycrystalline Iron. *Acta Metall.* **1965**, *13*, 591–604. [CrossRef]
41. Anderson, T.L. *Fracture Mechanics: Fundamentals and Applications*, 4th ed.; CRC Press: Boca Raton, FL, USA, 2017; Volume 76, ISBN 9780849316562.
42. Chen, J.H.; Wang, G.Z.; Wang, H.J. A Statistical Model for Cleavage Fracture of Low Alloy Steel. *Acta Mater.* **1996**, *44*, 3979–3989. [CrossRef]
43. Inoue, T.; Matsuda, S.; Okamura, Y.; Aoki, K. Fracture of a Low Carbon Tempered Martensite. *Trans. Jpn. Inst. Met.* **1970**, *11*, 36–43. [CrossRef]
44. Zhang, Y.; Yang, J.; Xiao, D.; Luo, D.; Tuo, C.; Wu, H. Effect of Quenching and Tempering on Mechanical Properties and Impact Fracture Behavior of Low-Carbon Low-Alloy Steel. *Metals* **2022**, *12*, 1087. [CrossRef]
45. Li, X.; Lu, G.; Wang, Q.; Zhao, J.; Xie, Z.; Misra, R.D.K.; Shang, C. The Effects of Prior Austenite Grain Refinement on Strength and Toughness of High-Strength Low-Alloy Steel. *Metals* **2022**, *12*, 28. [CrossRef]
46. Inoue, T.; Yin, F.; Kimura, Y.; Tsuzaki, K.; Ochiai, S. Delamination Effect on Impact Properties of Ultrafine-Grained Low-Carbon Steel Processed by Warm Caliber Rolling. *Metall. Mater. Trans. A Phys. Metall. Mater. Sci.* **2010**, *41*, 341–355. [CrossRef]
47. Cowie, J.G.; Azrin, M.; Olson, G.B. Microvoid Formation during Shear Deformation of Ultrahigh Strength Steels. *Metall. Trans. A* **1989**, *20*, 143–153. [CrossRef]
48. Maruyama, K.; Sawada, K.; Koike, J.I. Strengthening Mechanisms of Creep Resistant Tempered Martensitic Steel. *ISIJ Int.* **2001**, *41*, 641–653. [CrossRef]
49. Wen, P.; Chen, Z.; Yang, L.; Xie, Z.; Huang, D.; Liu, Z.; Luo, H. Ripening Kinetics of Bimodal-Sized Carbide via Boundary Diffusion in Coarse-Grained 9Cr Martensitic Steel. *Metall. Mater. Trans. A Phys. Metall. Mater. Sci.* **2022**, *53*, 4283–4295. [CrossRef]